

# Soft X-ray spectroscopy from image sequences with sub-100 nm spatial resolution

C. JACOBSEN,\* S. WIRICK,\* G. FLYNN† & C. ZIMBA‡

\*Department of Physics and Astronomy, State University of New York at Stony Brook, Stony Brook, NY 11794-3800, U.S.A.

†Department of Physics, State University of New York at Plattsburgh, Plattsburgh, NY 12901, U.S.A.

‡Polymer Division, MS 224/B108, National Institute of Standards and Technology, Gaithersburg, MD 20899, U.S.A.

**Key words.** Microanalysis, microspectroscopy, NEXAFS, spectromicroscopy, X-ray microscopy, XANES.

## Summary

A method is described whereby a sequence of X-ray images at closely spaced photon energies is acquired using a scanning transmission X-ray microscope, and aligned. Near-edge absorption spectra can then be obtained both from large, irregular regions, and from regions as small as the spatial resolution of the microscope (about 40 nm in the examples shown here). The use of the technique is illustrated in examination of a layered polymer film, a micrometeorite section, and an interplanetary dust particle section.

## Introduction

The absorption spectrum near an element's X-ray absorption edge contains considerable information on the chemical state of the element (Stöhr, 1992). This X-ray absorption near-edge structure (XANES) information can be exploited in spectromicroscopy by taking images at photon energies corresponding to absorption maxima and minima in different components of a specimen (Ade *et al.*, 1992). Soft X-ray microspectroscopy has proven useful for studies in areas including polymer science (Ade *et al.*, 1995) biology (Zhang *et al.*, 1996; Buckley *et al.*, 1997) and geochemistry (Cody *et al.*, 1995) (see also a recent review article on X-ray spectromicroscopy (Ade, 1998). Microspectroscopy (spectroscopy of small specimen regions) at higher photon energies has been used for studies in other areas, such as plant science (Schulze *et al.*, 1995). Interpretation of these images requires access to the absorption spectra of the various regions, and for heterogeneous specimens these are often obtained by microspectroscopy.

The usual practice in X-ray microspectroscopy has been to place a collimated or focused beam on a region of interest and vary the photon energy so as to acquire a transmission spectrum from the selected region (Zhang *et al.*, 1994; Sutton *et al.*, 1995). Typical of absorption spectroscopy, it is necessary to measure two spectra: one spectrum  $I(E)$  of transmission through the specimen and another measurement  $I_0(E)$  without the specimen so as to obtain the absorption spectrum as an optical density  $OD(E) = -\log[I(E)/I_0(E)]$ . For sample features of 200 nm or less in size, obtaining high quality spectra is challenging. When chromatic optics (such as Fresnel zone plates) are used, a focusing stage must be operated in synchronization with the monochromator. At the same time that the focus is adjusted, there should be no lateral motion of the photon beam on the sample. In practice, these limitations have made it difficult to acquire spectra from regions smaller than about 200 nm in width, whereas soft X-ray microscopes have an image resolution in the 30–50 nm range (Schneider *et al.*, 1995; Spector *et al.*, 1997). Furthermore, if the specimen transmission measurement  $I(E)$  and incident flux  $I_0(E)$  measurements are made separately, there is the potential for errors caused by time-dependent variations in incident flux.

In order to address these problems, we report here a different approach whereby a 'stack' of images of a small region is acquired at closely spaced intervals in X-ray energy. Each image is taken at the proper focus position on the sample plane, ensuring that there is no degradation in spatial resolution. Subsequent computer alignment of the images corrects for lateral motion of the X-ray beam on the sample, yielding a data cube with one dimension in X-ray energy and two dimensions in Cartesian position ( $x$  and  $y$ ). Spectra of single pixels or groupings of pixels can then be

Correspondence to: Chris Jacobsen. Tel: +1 516 632 8093; fax: +1 516 632 8101; e-mail: jacobsen@xray1.physics.sunysb.edu

easily extracted. This approach can be used for measuring the absorption spectrum of 50 nm regions, and should in principle work at the spatial resolution limit of the microscope.

This new 'stack' approach to measuring XANES spectra has been developed on the Stony Brook scanning transmission X-ray microscope (STXM) (Jacobsen *et al.*, 1991; Zhang *et al.*, 1994) at the X-1A beamline at the National Synchrotron Light Source. In principle, this method also could be used with a full-field transmission X-ray microscope (TXM), although in practice such instruments do not presently have sufficient energy resolution for quantitative XANES analysis, as will be discussed below. It is also conceptually quite similar to spectrum imaging in the STEM or energy-filtered TEM.

### Synchronization of X-ray energy and focus position

In microspectroscopy, the absorption spectrum from a small sample area is desired. If a zone plate optic is used to focus the X-rays, it is necessary to compensate for the chromatic nature of the zone plate in order to keep the sample at the focus of the zone plate as the photon energy  $E = hc/\lambda$  is varied. A zone plate of diameter  $d$  and outer zone width  $\delta_{rN}$  has a focal length  $f$  of

$$f = \frac{d\delta_{rN}}{\lambda} \quad (1)$$

and a Rayleigh resolution of  $\delta_t = 1.22\delta_{rN}$ . Changes in the wavelength  $\lambda$  should then be accompanied by changes in focus position according to

$$\frac{df}{d\lambda} = \frac{d\delta_{rN}}{\lambda^2}. \quad (2)$$

For an energy range of 40 eV at the carbon absorption edge, the focus range  $df$  can range from 77  $\mu\text{m}$  for a zone plate with  $d = 80 \mu\text{m}$  and  $\delta_{rN} = 30 \text{ nm}$ , to 232  $\mu\text{m}$  for a zone plate with  $d = 160 \mu\text{m}$  and  $\delta_{rN} = 45 \text{ nm}$ . To obtain spectra at the spatial resolution limit of the microscope, the focus position should be within the depth of field of the focus. For an optic with numerical aperture  $\text{NA} = \lambda/(2\delta_{rN}) = d/(2f)$ , the depth of field DOF is well approximated by

$$\text{DOF} = \frac{\lambda}{\text{NA}^2} = 4 \frac{\delta_{rN}^2}{\lambda} \quad (3)$$

which decreases as the square of increases in resolution. At the carbon edge,  $\text{DOF} = 0.8 \mu\text{m}$  for  $\delta_{rN} = 30 \text{ nm}$ , and  $\text{DOF} = 1.9 \mu\text{m}$  for  $\delta_{rN} = 45 \text{ nm}$ .

To avoid a degradation in spatial resolution, it is necessary to stay within a few micrometres of the focus. This offers a challenge for microspectroscopy as the focal length of the zone plate varies inversely with  $\lambda$ , while the typical grating monochromator disperses linearly in  $\lambda$ . One strategy is to adjust the monochromator, adjust the focus position, open the X-ray shutter for a predetermined time to measure the transmitted X-ray intensity, and close the

shutter, repeating this sequence at each wavelength until the full spectrum is measured. Experimentally, this is very inefficient because the time spent moving the monochromator, focusing stage, and shutter can be significantly greater than the 10–100 ms time needed to measure the transmitted X-ray intensity.

A more efficient strategy is to vary the monochromator and the zone plate position simultaneously while continuously acquiring data (Zhang *et al.*, 1994). However, if the monochromator and focus stage are both driven by stepping motors, it is difficult to synchronize the focus as required by Eq. (2) without specialized electronics. What is done instead is to tune the monochromator at a constant velocity over the desired wavelength range, and simultaneously adjust the focus over the desired range at a different constant velocity. Unfortunately, the deviation between the proper focal length  $f$  of Eq. (1) and a linear approximation  $f' = k\lambda$  can exceed the depth of focus DOF of Eq. (3), as is shown in Fig. 1. At X-ray energies where the deviation exceeds the depth of field, the sample will not be in focus and the spatial resolution will be degraded.

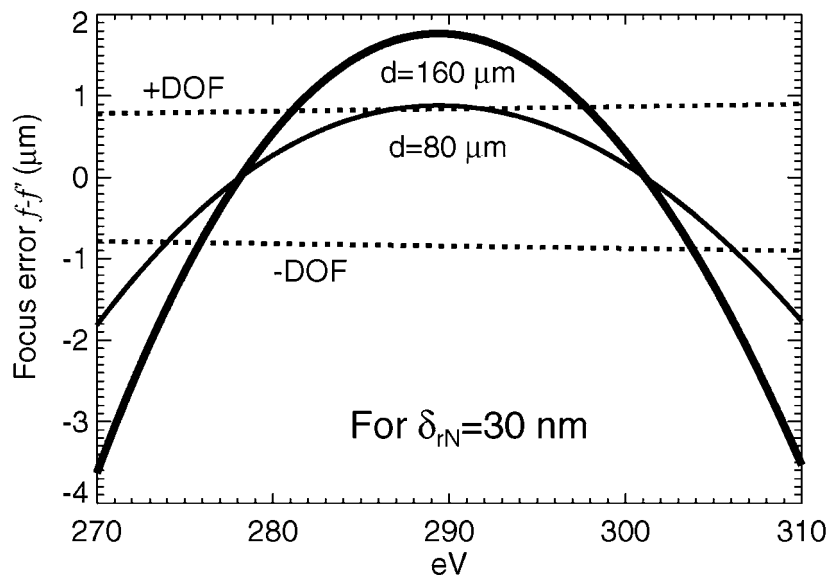
Even if the proper adjustment of focus with photon energy were provided, it would still be necessary to adjust the focus without any lateral motion of the specimen relative to the focused X-ray spot. If a crossed-roller bearing translation stage is used to adjust the focus position, there is significant transverse wobble that is presumably due to the roughness and noncircularity of the ball bearings and races. In the better stages that have been tested by us, this runout is approximately 0.2  $\mu\text{m}$ . An alternative is to use a flexure mechanism to guide the focus translation (Warwick *et al.*, 1997), although it is difficult to obtain long travel range and high stiffness simultaneously (so as to minimize vibrations) in flexure mechanisms. Even if a translation mechanism with insignificant transverse movement could be obtained, it would have to be aligned relative to the optical axis of the photon beam to an angular tolerance given by the transverse resolution  $1.22 \delta_{rN}$  divided by the focus range  $df$ , or about  $(36 \text{ nm}/100 \mu\text{m}) = 1$  minute of arc. While this might have to be done only once during microscope installation, it represents a significant challenge in aligning the microscope.

### Acquisition of spectromicroscopy stacks

Our approach to overcome these limitations is to take a series of images at closely spaced energies throughout the near-edge spectral region. These images can then be aligned to each other to eliminate lateral wobble, and spectra can then be obtained from regions within the stack of images.

When acquiring stacks of images at finely spaced X-ray energies, each image can take a minute or longer to be acquired. The time needed to move to the proper focus position after each change of the monochromator setting is an insignificantly small fraction of the image acquisition time. The exact focus position can be easily calculated from

Fig. 1. A linear approximation to the focus is not always sufficient for staying within the zone plate depth of field in microspectroscopy. The deviation between the proper  $f$  and the linearly approximated  $f' = k$  focal positions is shown as a function of X-ray energy for two different zone plates. The deviation  $f - f'$  is given by the solid curves for  $\delta_{rN} = 30$  nm outer zone width zone plates with diameters of 80 and 160  $\mu\text{m}$ , respectively. The depth of focus DOF is denoted by the two dotted lines representing the positive and negative limits of the depth of focus. When the focus deviation  $f - f'$  approaches or exceeds the depth of focus boundary, defocus effects will reduce the spatial resolution of the microspectroscopy measurement.



Eq. (1) and used to adjust the position of the zone plate at each X-ray energy for which an image is acquired, thus allowing the full spatial resolution of the microscope to be exploited. This method of operation also has other advantages. It is easy to reduce the per-pixel dwell time at photon energies where the beamline delivers high throughput or the sample shows strong contrast, and increase it at other energies to obtain sufficient signal-to-noise levels. It is also straightforward to collect only a few measurements at energies well below and above the absorption edge; these measurements are useful for normalizing a near-edge spectrum to tabulated values of the X-ray optical constants (see e.g. Boese *et al.*, 1997).

To accommodate this, routines written using the Interactive Data Language (IDL; Research Systems Inc., Boulder, CO) for this data acquisition method allow the user to specify multiple spectral regions that can have different energy step sizes and pixel dwell times. The microscope control computer carries out the sequence of monochromator adjustment, focus position adjustment and imaging for each of the photon energies in the stack. Typical image stacks involve 50–200 separate photon energies with pixel dwell times ranging between 1 and 50 ms, and image fields of  $50^2$ – $256^2$  pixels. Times for acquisition of these stacks have ranged from 30 min to 10 h, often during overnight operation with no experimenter present.

### Alignment of image stacks

As discussed above, when the focus position is changed, there is the potential for transverse motion of the image field. The solution adopted here is to align the images following the acquisition of a stack. In most cases this can be done automatically using a cross correlation similar to that done in automated electron tomography (Dierksen

*et al.*, 1992; Koster *et al.*, 1992). If image  $a$  has the same number of pixels and pixel size as image  $b$ , one obtains the cross correlation  $c$  from

$$|c| = |\mathcal{F}^{-1}\{\mathcal{F}(a) \cdot [\mathcal{F}(b)]^\dagger\}|, \quad (4)$$

where  $\mathcal{F}$  and  $\mathcal{F}^{-1}$  represent Fourier and inverse Fourier transforms, respectively, and  $\dagger$  represents the complex conjugate. The location of the peak value of  $|c|$  relative to the array centre then gives the shift of one image relative to another (Bracewell, 1986). Two methods can be used to find the position of the peak to sub-pixel accuracy (see e.g. Fig. 2):

- 1 A quadratic curve  $f(p) = k_1 + k_2p + k_3p^2$  can be calculated which intercepts the three pixels  $p$  centred at the peak of  $|c|$  in both the  $x$  and  $y$  directions, and the position of the peak in each direction is interpolated from  $-k_2/(2k_3)$ .

- 2 The cross correlation  $|c|$  is scaled from 0 to 1, and the centre of mass location of those pixels in  $|c|$  which have a value greater than 0.5 is found.

These two methods usually give results within a few tenths of a pixel of each other in tests on real images with  $\sim 3000$  photons per pixel. Note that because the absolute value of the cross correlation  $|c|$  is examined, the method usually gives proper alignment even in cases where the contrast is largely reversed due to differences in XANES contrast (see e.g. Ade *et al.*, 1992). In some cases it is helpful to edge-enhance the images prior to calculating  $|c|$ . To align  $N$  images, it is necessary to carry out  $2N + 1$  FFT operations and up to  $N - 1$  polynomial image shift operations. Although the alignment time will of course vary according to the number of pixels in the images, the number  $N$  of images and the computer used, a time of no more than a few minutes is common. The alignment can also be stored for subsequent reanalysis of the same stack.

With some datasets, automatic alignment is not always

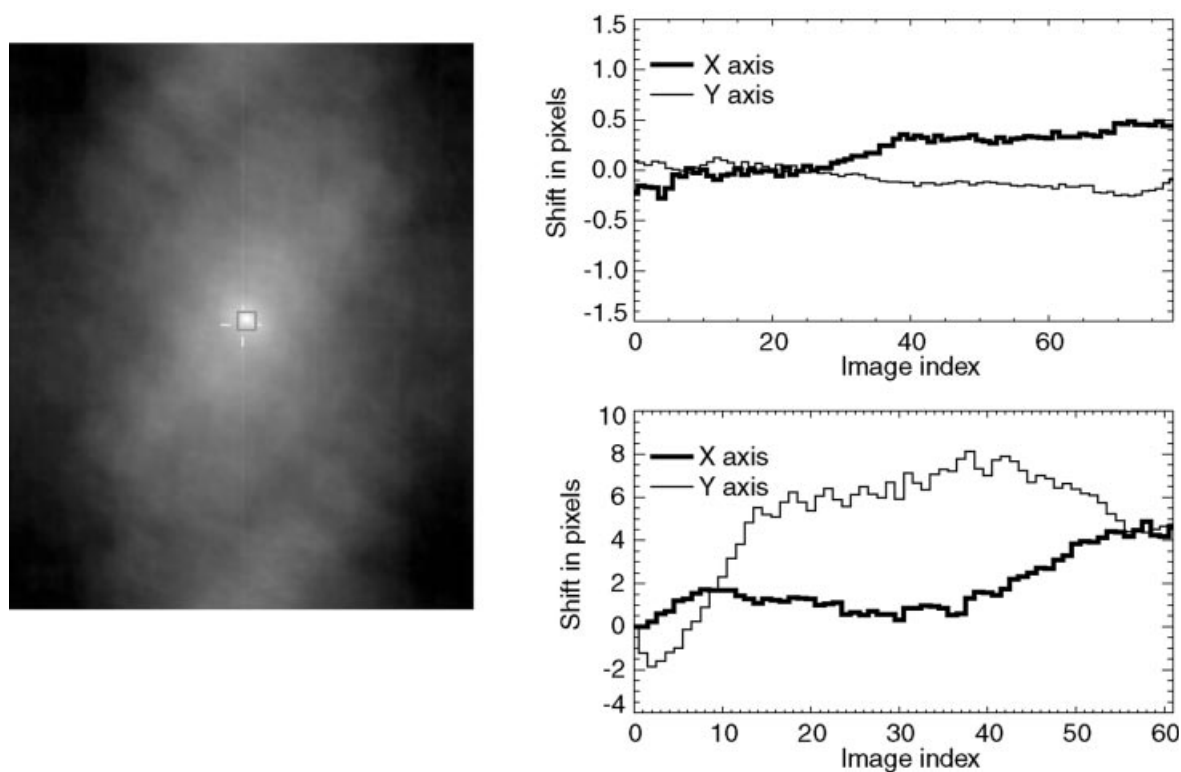


**Fig. 2.** Alignment of images using cross correlation. At left is shown the logarithm of the cross correlation image  $|c|$ . The centre of the array is indicated with four short white lines, whereas the position of the peak of the cross correlation image  $|c|$  is indicated with a small dark box (the box is placed over the nearest integer pixel position). At right are shown two examples of the shift in the centre position of images in stacks aligned using cross correlations and quadratic peak interpolation. The stack at upper right consisted of 79 images, each with  $250 \times 30$  pixels of 150 nm size, acquired over 2 h. The stack at lower right consisted of 62 images, each with  $180 \times 220$  pixels of 47 nm size, acquired over 6 h. The gradual drift of the image position centre in the example at lower right is probably due to some combination of misalignment of the focusing stage relative to the beam direction and thermal drifts in the specimen position. Abrupt changes between image centre positions are most likely caused by imperfections in the cross roller bearings of the translation stage used for focusing the zone plate.

successful in that spurious peaks can show up in the cross correlation image. Several strategies can be employed in such cases:

- It is often helpful to define a subregion of the reference image which contains particularly distinctive features. This subregion is windowed within the image with a Gaussian smothering of the subregion edges, and the entire image array as windowed is cross correlated with the rest of the images in the stack.
- If the  $x$ - $y$  position drift of the stack is reasonably small, one can direct the program to look for cross correlation peaks only within a certain pixel radius of the image centre.
- In less favourable cases, one must first align the stack manually by clicking on a feature which can be visually identified throughout the dataset. This manual alignment is usually good to one or two pixels; one can subsequently refine the alignment using the cross correlation method described above with a pixel radius limit, for example, three pixels to eliminate further problems with spurious cross correlation peaks.

Finally, if there is drift of the sample position during the acquisition of an image, this will result in image distortion. This can be compensated for somewhat by realigning the dataset on a particular feature in the specimen for analyses only in the immediate neighbourhoods of this feature, and then realigning on a different feature for analysis in a different region.

### Obtaining spectra

After the sequence of images has been aligned, the data can be used for microspectroscopic analysis. To obtain the absorption spectrum of the sample, it is necessary to obtain an incident flux spectrum  $I_0(E)$ . The best approach is to include a hole in the sample within the imaged region and to use the spectrum extracted from the hole as the incident flux spectrum. Alternatively, a region of the embedding matrix can be used, provided that the embedding material is of uniform thickness (e.g. sulphur used to embed interplanetary dust particles, or ice surrounding frozen hydrated samples). In either case, the incident flux spectra are

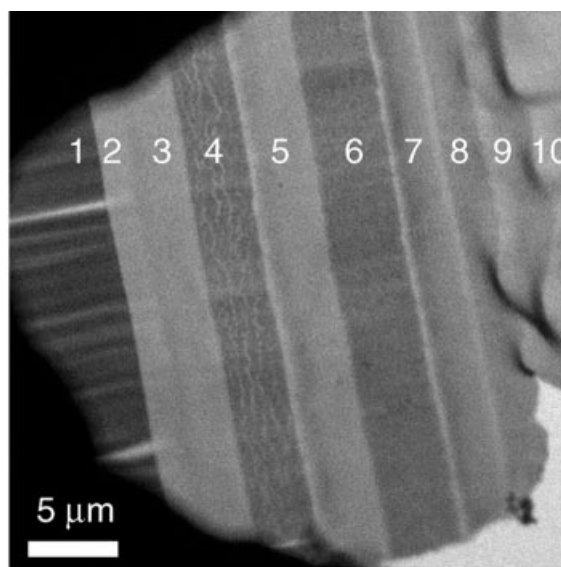
measured simultaneously with the sample spectra, so that flux variations occurring on the time scale of a single image acquisition are normalized away. Regions of  $I(E)$  and  $I_0(E)$  pixels are separately defined by the user of the stack analysis software through the use of the computer mouse to designate single pixels, regions of several pixels in size, or several spatially separated regions of pixels (see e.g. Fig. 7). The average flux  $I_0(E_i)$  and  $I(E_i)$  is then obtained by averaging the signal over all of these pixels for the image at energy  $E_i$ , and the optical density  $OD(E)$  is then determined from this operation carried out over the set of images.

A third, and less preferable, alternative to obtaining the incident flux spectrum  $I_0(E)$  is to acquire high quality reference spectra before and after acquisition of the stack of images. This third approach can suffer from variations in X-ray intensity that occur during the stack data acquisition

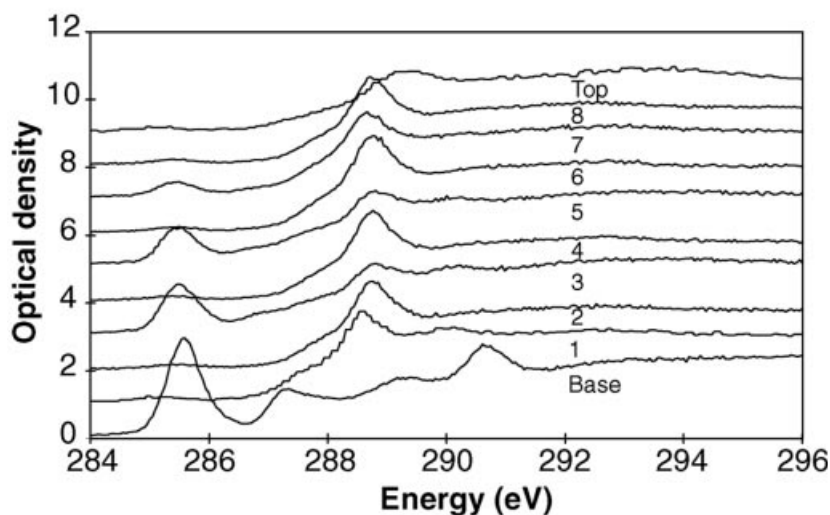
time, especially if these variations are not constant across all photon energies.

#### Example: phase separation in a polymer laminate

The general utility and improved spatial resolution for the acquisition of XANES spectra from image stacks is illustrated in the characterization of a multilayer polymer film. The sample is a 70 nm thick cross-section of a prototype photographic film composed of 10 layers, each of which is clearly evident in the X-ray image taken at 287.0 eV (Fig. 3). The film base (layer 1) is a 125  $\mu\text{m}$  sheet of polycarbonate upon which all the other layers are sequentially coated. Layer 2 is a subcoat of urethane acrylic copolymer while layers 3, 5, 7 and 9 are barrier layers of acrylic copolymer. Layers 4 and 6 are photographic imaging layers of cyan and magenta dyes, respectively, in



**Fig. 3.** X-ray micrograph (top) of a 10-layer polymer laminate obtained using 287.0 eV (4.320 nm) photons. The sample is a 70 nm thick cross-section of a prototype photographic film consisting of 10 layers, each numerically labelled in the figure. The size of the image is approximately  $30 \times 30 \mu\text{m}$  with a spatial resolution of 75 nm per pixel. The image was obtained using a dwell time of 5 ms/pixel for a total acquisition time of 13.3 min. Absorption spectra from the various layers are shown below, as obtained using spot microspectroscopy.



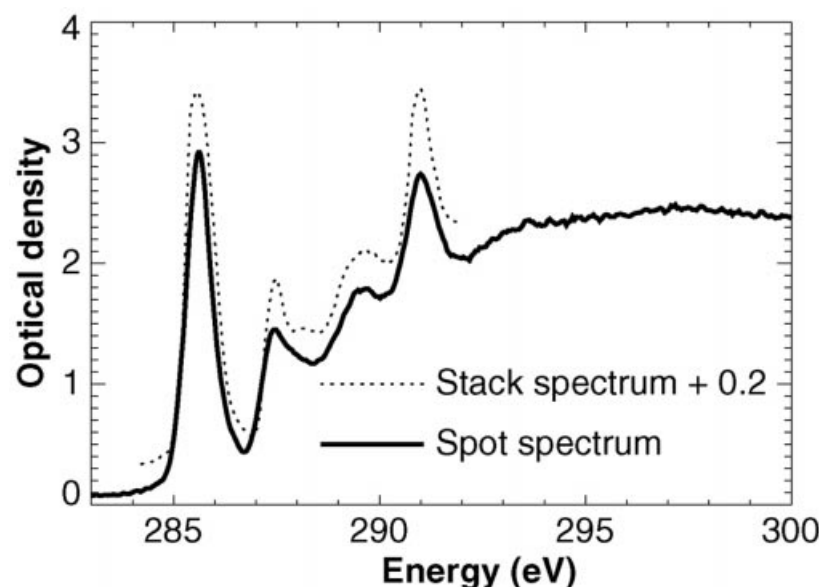


Fig. 4. Essentially identical absorption spectra of polycarbonate are obtained from spot microspectroscopy and spectromicroscopy image 'stack' methods. These two spectra are both from the layer 1 region of Fig. 3.

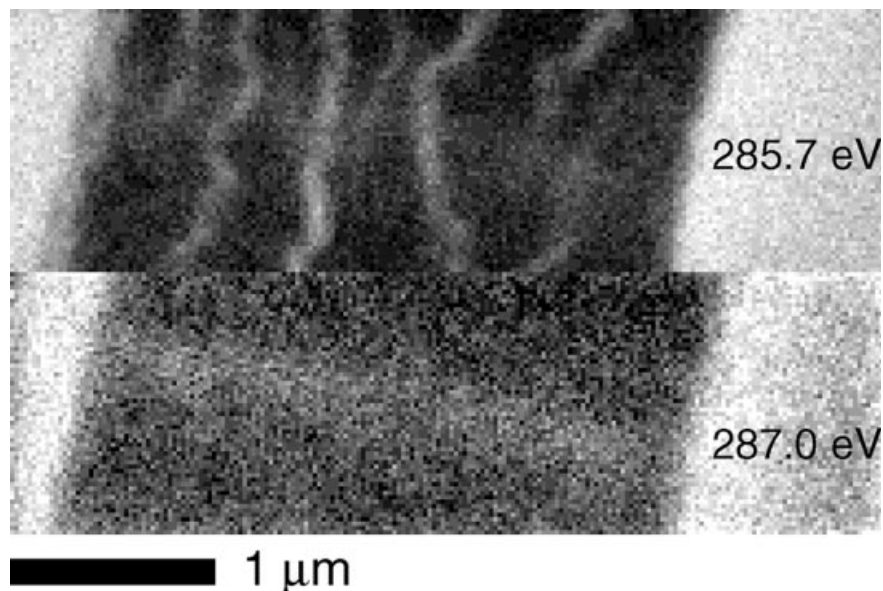
polymethylmethacrylate and polyvinyl alcohol. Layer 8 is the third photographic imaging layer of yellow dye in polymethylmethacrylate and polyvinyl pyrrolidone. Layer 10 is a protective overcoat of ethyl cellulose.

Spectra from Layer 1, the base film of polycarbonate (PC), were obtained using both conventional spot microspectroscopy and data extracted from an image stack (see Fig. 4). The spot spectrum was obtained by focusing on a small spot in the PC layer and simultaneously scanning the monochromator from 4.0000 to 4.4000 nm in  $8 \times 10^{-4}$  nm steps (or 309.96 to 281.78 eV in 0.05 eV steps) with a dwell time of 60 ms per step, and simultaneously scanning the zone plate focus over a 55  $\mu\text{m}$  range (as required for  $d = 80 \mu\text{m}$  and  $\delta_{rN} = 55 \mu\text{m}$ ). The stack spectrum was obtained by acquiring images over an energy range of 292.0 to 284.0 eV in 0.1 eV steps with a dwell time of 10 ms per pixel in each image. As Fig. 4 shows, these two spectra are quite similar in appearance. The stack spectrum has a somewhat lower signal-to-noise ratio, but this can be enhanced by averaging the spectra obtained from many pixels in the image. In addition, the resonances near 285.5 eV and 287.5 eV appear to have slightly lower optical density relative to that of the resonance near 291 eV. This slight difference is possibly due to radiation damage in the polymer (Zhang *et al.*, 1995; Rightor *et al.*, 1997). It should be noted that there is no intrinsic difference in radiation damage between stack spectra and spot-mode spectra at equal spatial resolution and spectral quality; however, if the experimenter chooses to make use of the potential in stack mode for higher spatial resolution, the radiation dose delivered to the specimen will of course be increased.

Of particular interest in the image of Fig. 3 is the fine structure that is present in layer 4. This photographic imaging layer is composed in mass percentages of 39%

dye, 23% polymethylmethacrylate (PMMA), 20% polyvinyl alcohol (PVA), 10% sodium dioctyl sulfosuccinate, 6% t-butylhydroxyquinone and 2% other miscellaneous components. As illustrated in Fig. 5, the contrast of the fine structure of layer 4 changes with X-ray energy, even to the point of appearing completely uniform at some energies. The fine structures seen in Fig. 5 therefore cannot be due to physical cracks involving mass density nonheterogeneities (as confirmed by the lack of such features in transmission electron micrographs). Instead, they must arise from chemical differences at a very fine spatial scale. Prior to the development of the stack approach for the acquisition of XANES spectra, it was not possible to obtain unequivocal spectral data from features this small. Using the stack method, X-ray absorption spectra of the fine structures and the surrounding matrix were easily obtained (see Fig. 6). Of the four most prominent spectral features, the three absorption resonances near 287.0, 289.0 and 290.5 eV exhibit similar intensities between the fine structure and the matrix. These strongest of these absorption resonances, at 289.0 eV, is due to the PMMA, whereas the other two weaker resonances likely arise from the PVA. Thus, the relative concentration of PMMA and PVA is very similar in both the fine structure and the surrounding matrix. The largest difference in the spectra shown in Fig. 6 is the intensity of the XANES absorbance near 285.5 eV. This absorption is most likely to arise from an aromatic species (most likely the photographic dye). The difference in resonance intensity indicates that the aromatic species, although present in both areas, has a significantly lower concentration in the areas where fine structure are seen. It is clear from these measurements that there is a preferential depletion of an aromatic species from the areas of fine structure and into the surrounding material within layer 4.

**Fig. 5.** XANES images of layer 4 with (upper) and without (lower) contrast between the fine structure (lighter regions) and the surrounding matrix (darker regions). An absorption spectrum of the fine structures is shown in Fig. 6. The upper and lower images were obtained using X-ray photon energies of 285.7 eV and 287.0 eV, respectively. Both images were acquired as part of a stack acquisition where 100 separate images were measured from 292.0 to 282.0 eV in 0.1 eV intervals of photon energy. A  $4.20 \times 1.38 \mu\text{m}$  field is shown with an average pixel size of 22 nm (representing Nyquist sampling with the  $\delta_{rN} = 40 \text{ nm}$  zone plate used). The pixel dwell time was 5 ms, so each  $200 \times 60$  pixel image took approximately 1 min to acquire.



#### Example: Mars meteorite

In 1996, McKay *et al.* (1996) examined material, dominated by carbonates, found along fracture surfaces in the ALH84001 meteorite believed to be from Mars. They

detected polycyclic aromatic hydrocarbons (PAHs), which are frequently produced by the decay of living material, 'in the highest concentrations in the regions rich in carbonates' (McKay *et al.*, 1996). They also found magnetite and Fe-S grains, similar in size and shape to those produced by

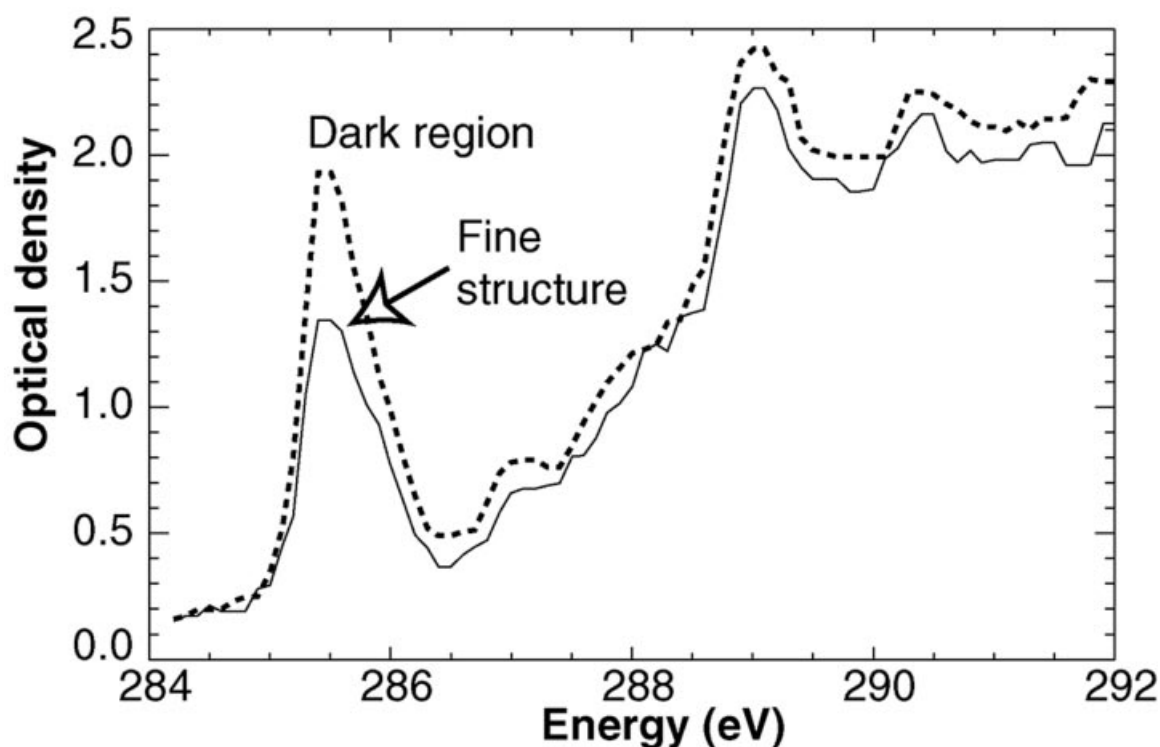


**Fig. 6.** XANES spectra of the fine structure and surrounding matrix within layer 4. The lower spectrum is from one pixel of the fine structure present in the upper image of Fig. 5 (the fine structure), while the upper spectrum is from seven pixels of the surrounding darker areas. The difference between the two regions can be seen to be primarily in their absorption at 285.5 eV, whereas the absorption at other energies is nearly identical. Both spectra were extracted from a stack data set of 100 images from 292.0 to 282.1 eV in 0.1 eV intervals of photon energy.

terrestrial bacteria, occurring in rims surrounding carbonate globules. This close spatial association of a possible indicator of liquid water (carbonates, which frequently precipitate from water), mineral grains consistent in size and shape with those produced by bacteria, and hydrocarbons consistent with biological decay material led them to suggest that ALH84001 contained evidence of possible ancient biological activity on the planet Mars. However, the PAHs were detected by laser desorption laser ionization mass spectrometry, using an instrument with a sampling beam-spot 50  $\mu\text{m}$  in size (McKay *et al.*, 1996). The analysis spot was comparable to the size of entire carbonate globules ( $\sim 50\text{--}100\ \mu\text{m}$ ), and much larger than the rims ( $\sim 5\text{--}10\ \mu\text{m}$  thick) or the individual magnetite and Fe–S crystals (tens of nanometres) of possible biogenic origin. In addition, their technique was sensitive only to PAHs, not other organic molecules which are less stable in the laser desorption process but potentially more biologically significant.

Our objectives are to determine the spatial association of carbon-bearing compounds with the mineral phases in ALH84001 and to determine if organic carbon other than PAHs is present in the sample. The spatial resolution of the STXM is about 1000 times better than that available to McKay *et al.* (1996); that is, 50 nm for the STXM vs. 50  $\mu\text{m}$  for the laser desorption laser ionization mass spectrometric technique. The stack imaging technique provided two improvements over our prior examination of the ALH84001 carbonates with the STXM (Flynn *et al.*, 1998c). First, we are now able to obtain C-XANES spectra integrated over designated regions of interest on the sample, allowing us to compare average carbon abundances in distinct subunits of the sample. Second, we can now employ the 50 nm spatial resolution of the STXM to investigate associations between organic matter and the mineral phases, which are frequently only tens of nanometres in size, in the ALH84001 rim. This should allow us to address questions such as whether magnetites have coatings of organic matter.

Chips of ALH84001 were embedded in elemental sulphur, and a series of ultramicrotome thin sections were deposited on an SiO substrate (Flynn *et al.*, 1998c). Several sections included a small ( $\sim 2 \times 2\ \mu\text{m}$ ) area of rim material attached to an  $\sim 8\ \mu\text{m}$  globule fragment, preserving the spatial associations between the rim and the globule (see Fig. 7). Transmission electron microscope (TEM) examination of the section analysed indicates it contains three distinct regions which we denote as follows:

Rim: fine-grained rim material consisting of carbonate, magnetite and rare sulphides.

Globule: coarse-grained carbonate in the chip interior.

Porous: coarse-grained, porous carbonate and sparse, fine-grained magnetite.

The porous region lies between the globule and rim regions, as is shown in Fig. 7.

For X-ray microscopy studies, a stack consisting of 163 images was taken over the range 270–310 eV, with an energy spacing of  $\sim 0.1\ \text{eV}$  in the pre-edge region (Flynn *et al.*, 1998b). After the images were aligned, the carbon XANES spectra of each of the three morphologically distinct regions were extracted from the stack (see Fig. 7). The rim material showed four strong absorption peaks. The three absorption peaks at 285, 286.2 and 288 eV are similar to the peaks we have detected from the organic extracts from other meteorites. We therefore identify this material as organic (e.g. from polycyclic aromatic hydrocarbons). Spot analyses of this ALH84001 sample demonstrate that these three peaks are reproducible in energy and relative intensity at various spots on the sample (Flynn *et al.*, 1998c). The fourth peak, at 290 eV, is consistent with the spectrum of a carbonate standard. The globule material, and the porous carbonate which separates the rim from the globule interior, both show the same four absorption peaks. In each carbon XANES spectrum we can measure the ratio of the absorption at 290 eV to that at 288 eV to monitor the ratio of carbonate to organic carbon. A comparison of the average carbon XANES spectrum over the carbonate globule with the average over the rim indicates that the rim has a higher ratio of organic carbon to carbonate than does the globule. The porous carbonate appears to have approximately the same ratio of organic carbon to carbonate as the globule interior. The highest ratio of organic carbon to carbonate was found in isolated spots within the rim. We therefore have confirmed the result of McKay *et al.* (1996) that high concentrations of organic matter are associated with the carbonate in the ALH84001 meteorite, and extended their measurement by demonstrating that the highest concentration of organic carbon is in the rim material, where the magnetite and sulphide crystals that McKay *et al.* speculate are of possible biogenic origin are concentrated.

Further efforts to determine the specific minerals with which this organic matter are associated will require overlaying STXM maps showing the spatial distribution of the organic phase on the TEM maps showing the locations of specific non-carbon-bearing minerals such as magnetite and Fe–S.

### Example: interplanetary dust particles

Interplanetary dust particles (IDPs), typically  $\sim 10\ \mu\text{m}$  in diameter, are small fragments from asteroids and comets that survive atmospheric entry, frequently without being heated above 400 to 600 °C. IDPs are recovered from the Earth's stratosphere by NASA stratospheric sampling aircraft (Brownlee, 1985). Modelling by Anders (1989) indicates that interplanetary dust may have been an important source of organic matter on the early Earth, providing some of the pre-biotic organic compounds



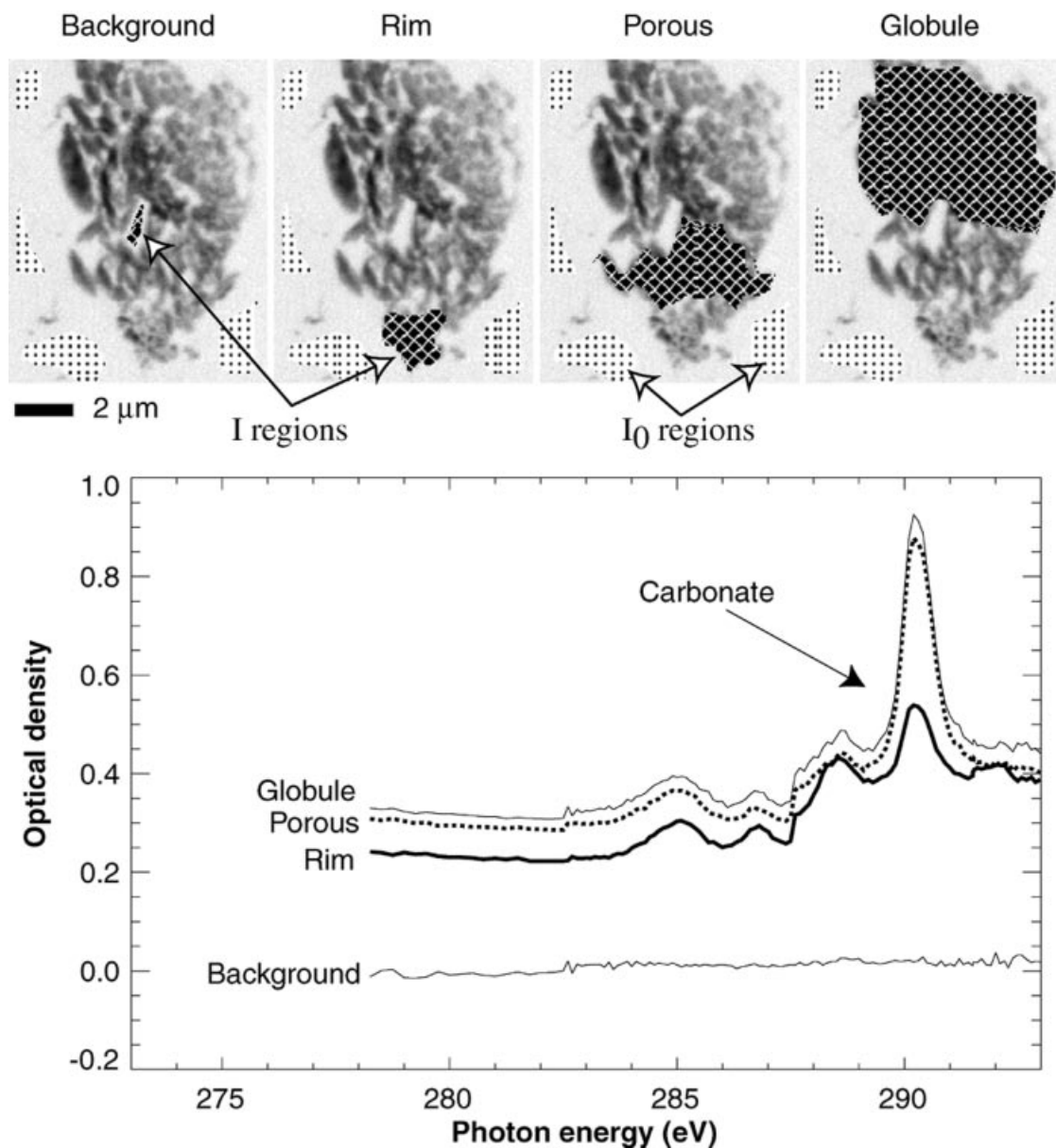


**Fig. 7.** Images (top) and spectra (bottom) of a thin section of a chip from the ALH84001 meteorite in which McKay *et al.* (1996) have suggested contains signs of past biological activity on Mars. The image shown from the stack was taken at a photon energy of 284.0 eV, with a pixel size of 48 nm. The same  $I_0$  regions (X-ray transmission through the sulphur embedding material and SiO substrate) were used for all four analysis regions, as shown. Different analysis regions were selected (two are indicated by arrows) to highlight a background region within the specimen, the carbonaceous-rich rim which is rich in polycyclic aromatic hydrocarbons (PAHs), and the porous and globule regions of the meteor chip. The corresponding absorption spectra indicate that the rim has a higher ratio of organic material to carbonate.

required for the development of life on Earth. Similar modelling for Mars indicates the IDPs contributed a higher surface density of non-pyrolized organics to the early surface of Mars than to the Earth, suggesting that organic carbon carried to Mars by IDPs may have been important in any possible development of life on Mars (Flynn, 1996).

The IDPs collected by NASA from the Earth's stratosphere

are carbon-rich, containing an average of about 13 wt.% carbon (Keller *et al.*, 1994). However, the ratio of elemental to organic carbon in the IDPs is not well established. Both electron energy loss spectroscopy (EELS) measurements (Keller *et al.*, 1994) and carbon XANES measurements (Bajt *et al.*, 1996) indicate that some IDPs are dominated by poorly graphitized or amorphous elemental carbon rather

than organic carbon. To determine the importance of IDPs as a contributor of pre-biotic organic matter to the early surfaces of the Earth and Mars, and in the present era to the surfaces of Europa and Titan (which some have recently speculated have favourable conditions for the development of life), we have begun a project to determine the carbon abundances in IDPs, map the spatial distribution of that carbon in each particle, and determine the carbon bonding state in each carbon-rich region of the IDP.

Two of the first three IDPs we examined using the STXM were dominated by elemental carbon (e.g. poorly graphitized or amorphous carbon), rather than organic carbon

(i.e. carbon compounds containing hydrogen and oxygen) (Bajt *et al.*, 1996). However, because of the problems with spot microspectroscopy described earlier, we were only able to obtain C-XANES spectra of relatively large carbon-bearing regions,  $\sim 200$ – $500$  nm in size, in those IDPs. The stack imaging technique has allowed us to extend those measurements to a finer spatial scale, which is important because the most primitive of the IDPs (those which have experienced minimal thermal and aqueous alteration) contain mineralogical subunits only tens of nanometres in size.

We have, thus far, examined six IDPs using the stack

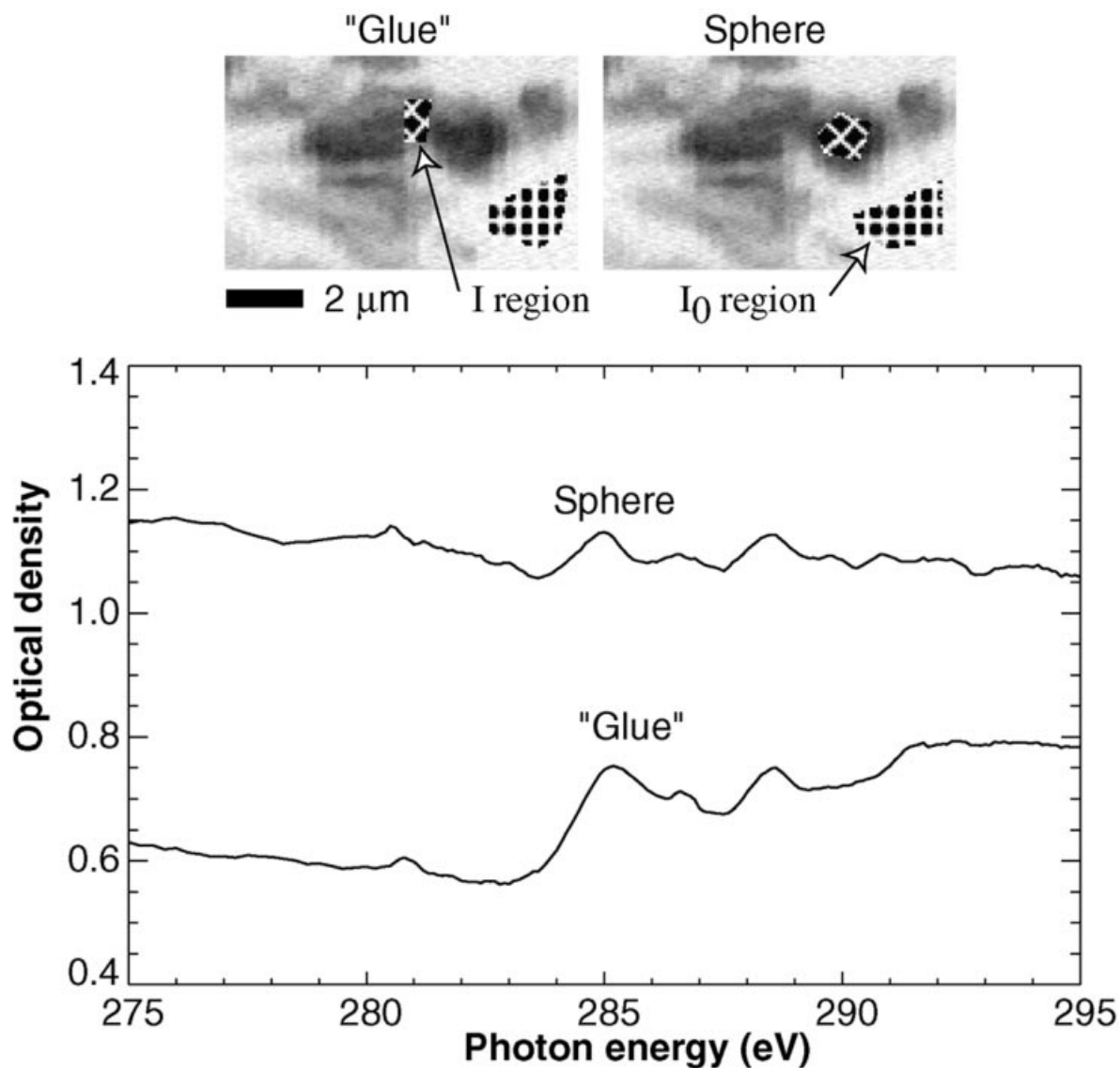


Fig. 8. Images (top) and absorption spectra (bottom) of a region of the interplanetary dust particle L2009J4. The image shown from the stack was taken at a photon energy of  $296.25$  eV, with a pixel size of  $24$  nm. The larger grains of material (including the spherical grain at right) show relatively little carbon content, whereas the material surrounding the spheres (labelled 'glue' in the image) shows more pronounced carbon content, as indicated by the increase in absorption near the carbon edge in the 'glue' spectrum.

imaging technique (Flynn *et al.*, 1998a). We identified three distinct morphologies of carbon in the particles:

- 1 individual, sub-micrometre size carbon-rich grains
- 2 large ( $\sim 0.5 \mu\text{m}$  or larger) distributed regions of carbon, sometimes surrounding non-carbonaceous grains
- 3 thin coatings (100–200 nm) of carbon-bearing material on the surfaces of non-carbonaceous grains.

These thin coatings of carbon-bearing material are particularly significant because their appearance is as of a 'glue' which holds the non-carbonaceous subunits of the IDPs together. Figure 8 shows an image of a small region of the interplanetary dust particle L2009J4. The spheres are non-carbonaceous, as shown by the absence of a carbon absorption edge in the C-XANES spectrum. However, the  $\sim 100$  nm thin region separating two spheres shows a significant increase in absorption at the carbon K-edge. There are hints of pre-edge peaks (see Fig. 4) in these spectra at energies similar to those which we have obtained for the carbon extracted from primitive meteorites. Because this carbon is part of the structure that appears to be holding the non-carbonaceous grains together, we believe this carbon must be indigenous to the IDPs. Without stack-imaging we were unable to obtain C-XANES spectra of these thin coatings, because the beam would drift off the coating during the analysis.

The preliminary stack analyses of IDPs indicate that organic carbon is a common component of IDPs, and that IDPs may have been an important source of pre-biotic organic matter on the early Earth.

## Conclusion

The stack method represents a significant improvement in the ability to measure XANES spectra from sample regions below 200 nm using scanning transmission X-ray microscopes. Based upon the examples cited above and much other work not described here, it is clear that the stack method can provide XANES spectra from regions as small as a single spatial resolution element, or better than 50 nm at present. Furthermore, because the stack method allows images to be acquired at finely spaced intervals of photon energy, it is possible to observe subtle features in both images and spectra. These subtle and detailed features would be far less evident and even unobserved using the more traditional approach of acquiring images at only a handful of selected energies and spectra at only a few locations in the sample. With the wealth of information now available using the stack method, it is clear that chemometric analysis can be used to give further insight into the spatial distribution and concentration variations of individual chemical species in complex multicomponent samples. This should lead to significant improvements in the sensitivity and chemical selectivity of XANES microscopy.

In principle, the stack method could be used in full-field

transmission X-ray microscopes (TXM) as well as in scanning transmission X-ray microscopes (STXM). As many XANES spectral absorbances have intrinsic widths of  $\sim 0.2$  eV, accurate measurement of their peak heights require a monochromator energy resolution of  $\sim 0.1$  eV if possible, or a spectral resolving power of 3000 or more at the carbon absorption edge (see e.g. Buckley *et al.*, 1997). STXMs are well-suited for this microspectroscopy demand, as high resolution grating monochromators are well matched to the requisite coherent illumination by a small collimated photon beam. Compared to STXMs, TXMs are presently less suitable for microspectroscopy. In practice, TXMs have a spectral resolving power of about  $E/\Delta E \approx 300$  in normal operation, or as high as  $E/\Delta E \approx 1500$  for  $1\text{--}2 \mu\text{m}$  image fields (Neuhäusler, 1996), although novel condenser optic schemes may improve this in the future (Niemann, 1998).

The spectral image stack method described here has become one of the standard data acquisition methods available on the Stony Brook STXM (Jacobsen *et al.*, 1991; Zhang *et al.*, 1994) at beamline X-1A at the National Synchrotron Light Source. The method, and an adaptation of the software, has since been put into practice with the cryo STXM at X-1A (Maser *et al.*, 1998) and a STXM at the Advanced Light Source (Warwick *et al.*, 1997).

## Acknowledgements

We thank Adam Hitchcock, Janos Kirz, Ulrich Neuhäusler, Angelika Osanna and Stephen Urquhart for many helpful discussions. This work was carried out at the X-1A beamline of the National Synchrotron Light Source (NSLS) at Brookhaven National Laboratory. The NSLS is supported by the U.S. Department of Energy (DoE), Office of Basic Energy Science, Divisions of Materials Science and Chemical Sciences (DE-AC02-76CH00016). Further support for the development of the X-1A STXM by the SUNY-Stony Brook X-ray Microscopy group was provided by the DoE, Office of Biological and Environmental Science (DE-FG02-89ER60858) and NSF (DBI-9605045). The X-ray zone plates were developed in collaboration with Lucent Technologies with support from NSF (ECS-9510499).

## References

- Ade, H., Zhang, X., Cameron, S., Costello, C., Kirz, J. & Williams, S. (1992) Chemical contrast in X-ray microscopy and spatially resolved XANES spectroscopy of organic specimens. *Science*, **258**, 972–975.
- Ade, H., Smith, A.P., Cameron, S., Cieslinski, R., Mitchell, G., Hsiao, B. & Rightor, E. (1995) X-ray microscopy in polymer science: prospects of a 'new' imaging technique. *Polymer*, **36** (9), 1843–1848.
- Ade, H. (1998) X-ray spectromicroscopy. *Experimental Methods in*

- the Physical Sciences*, Vol 32 (ed. by R. Celotta and T. Lucatorto), pp. 225–262. Academic Press, New York.
- Anders, E.A. (1989) Pre-biotic organic matter from comets and asteroids. *Nature*, **342**, 255–257.
- Bajt, S., Chapman, H., Flynn, G.J. & Keller, L.P. (1996) Characterization in individual interplanetary dust particles with a scanning transmission x-ray microscope. *Lunar Planet. Sci. XXVII*, 57–58.
- Boese, J., Osanna, A., Jacobsen, C. & Kirz, J. (1997) Carbon edge XANES spectroscopy of amino acids and peptides. *J. Electron Spectrosc. Relat. Phenom.* **85**, 9–15.
- Bracewell, R.N. (1986) *The Fourier Transform and its Applications*, 2nd edn. McGraw-Hill, New York.
- Brownlee, D.E. (1985) Cosmic dust collection and research. *Annu. Rev. Earth Planet. Sci.* **13**, 147–173.
- Buckley, C.J., Khaleque, N., Bellamy, S.J., Robins, M. & Zhang, X. (1997) Mapping the organic and inorganic components of tissue using NEXAFS. *J. Physique*, **IV 7** (C2 Part 1), 83–90.
- Cody, G.D., Botto, R.E., Ade, H., Behal, S., Disko, M. & Wirick, S. (1995) Inner-shell spectroscopy and imaging of a subbituminous coal: in-situ analysis of organic and inorganic microstructure using C(1s)-, Ca(2p)-, and Cl(2s)-NEXAFS. *Energy Fuels*, **9**, 525–533.
- Dierksen, K., Typke, D., Gegerl, R., Koster, A.J. & Baumeister, W. (1992) Towards automatic electron tomography. *Ultramicroscopy*, **40**, 71–87.
- Flynn, G.J. (1996) The delivery of organic matter from asteroids and comets to the early surface of Mars. *Earth, Moon, and Planets*, **72**, 469–474.
- Flynn, G.J., Keller, L.P., Jacobsen, C. & Wirick, S. (1998a) Carbon and potassium mapping and carbon bonding state measurements on interplanetary dust. *Meteoritics Planetary Science*, **33** (Supplement) (4), A50–A51.
- Flynn, G.J., Keller, L.P., Jacobsen, C. & Wirick, S. (1998b) Carbon in Allan Hills 84001 carbonate and rim. *Meteoritics Planetary Science*, **33** (Supplement) (4), A50.
- Flynn, G.J., Keller, L.P., Miller, M.A., Jacobsen, C. & Wirick, S. (1998c) Organic compounds associated with carbonate globules and rims in the ALH84001 meteorite. *Lunar and Planetary Science*, **XXIX**, Houston, TX, USA. Lunar and Planetary Institute. Abstract 1156.
- Jacobsen, C., Williams, S., Anderson, E., Browne, M.T., Buckley, C.J., Kern, D., Kirz, J., Rivers, M. & Zhang, X. (1991) Diffraction-limited imaging in a scanning transmission X-ray microscope. *Opt. Comm.* **86**, 351–364.
- Keller, L.P., Thomas, K.L. & McKay, D.S. (1994) Carbon in primitive interplanetary dust particles. *Analysis of Interplanetary Dust, AIP Conference Proceedings Vol. 310* (ed. by M. E. Zolensky, T. L. Wilson, F. J. M. Rietmeijer and G. J. Flynn), pp. 159–164. American Institute of Physics, New York.
- Koster, A.J., Chen, H., Sedat, J.W. & Agard, D.A. (1992) Automated microscopy for electron tomography. *Ultramicroscopy*, **46**, 207–227.
- Maser, J., Jacobsen, C., Kirz, J., Osanna, A., Spector, S., Wang, S. & Warnking, J. (1998) Development of a cryo scanning x-ray microscope at the NSLS. *X-ray Microscopy and Spectromicroscopy* (ed. by J. Thieme, G. Schmahl, E. Umbach and D. Rudolph), pp. I-35–44. Springer-Verlag, Berlin.
- McKay, D.S., Gibson, E.K., Thomaskeprta, K.L., Vali, H., Romanek, C.S., Clemett, S.J., Chillier, X.D.F., Maechling, C.R. & Zare, R.N. (1996) Search for past life on Mars: possible relic biogenic activity in Martian meteorite ALH84001. *Science*, **273**, 924–930.
- Neuhäusler, U. (1996) Untersuchungen zum elementspezifischen Kontrast an Absorptionskanten mit dem Röntgenmikroskop. Diplom thesis, Georg-August-Universität Göttingen, Germany.
- Niemann, B. (1998) High numerical-aperture X-ray condensers for transmission X-ray microscopes. *X-ray Microscopy and Spectromicroscopy* (ed. by J. Thieme, G. Schmahl, E. Umbach and D. Rudolph), pp. I-35–44. Springer-Verlag, Berlin.
- Rightor, E.G., Hitchcock, A.P., Ade, H., Leapman, R.D., Urquhart, S.G., Smith, A.P., Mitchell, G., Fischer, D., Shin, H.J. & Warwick, T. (1997) Spectromicroscopy of poly(ethylene terephthalate): comparison of spectra and radiation damage rates in x-ray absorption and electron energy loss. *J. Phys Chem. B* **101** (11), 1950–1960.
- Schneider, G., Schliebe, T. & Aschoff, H. (1995) Cross-linked polymers for nanofabrication of high-resolution zone plates in nickel and germanium. *J. Vacuum Sci. Technol. B* **13** (6), 2809–2812.
- Schulze, D.G., McCay-Buis, T., Sutton, S.R. & Huber, D.H. (1995) Manganese oxidation states in *Gaeumannomyces*-infested wheat rhizospheres probed by micro-XANES spectroscopy. *Phytopathology*, **85**, 990–994.
- Spector, S., Jacobsen, C. & Tennant, D. (1997) Process optimization for production of sub-20 nm soft x-ray zone plates. *J. Vacuum Sci. Technol. B* **15** (6), 2872–2876.
- Stöhr, J. (1992) *NEXAFS Spectroscopy*. Springer-Verlag, Berlin.
- Sutton, S.R., Bajt, S., Delaney, J., Schulze, D. & Tokunaga, T. (1995) Synchrotron X-ray fluorescence microprobe: quantification and mapping of mixed valence state samples using micro-XANES. *Rev. Sci. Instrum.* **66** (2), 1464–1467.
- Warwick, T., Ade, H., Hitchcock, A.P., Padmore, H., Rightor, E.G. & Tonner, B.P. (1997) Soft X-ray spectromicroscopy development for materials science at the Advanced Light Source. *J. Electr. Spectrosc. Rel. Phenom.* **84**, 85–98.
- Zhang, X., Ade, H., Jacobsen, C., Kirz, J., Lindaas, S., Williams, S. & Wirick, S. (1994) Micro-XANES: chemical contrast in the scanning transmission X-ray microscope. *Nucl. Instrum. Methods Phys. Res. A* **347**, 431–435.
- Zhang, X., Jacobsen, C., Lindaas, S. & Williams, S. (1995) Exposure strategies for PMMA from *in situ* XANES spectroscopy. *J. Vac. Sci. Technol. B* **13** (4), 1477–1483.
- Zhang, X., Balhorn, R., Mazrimas, J. & Kirz, J. (1996) Mapping and measuring DNA to protein ratios in mammalian sperm head by XANES imaging. *J. Struct. Biol.* **116**, 335–344.